Nonstationary Trapped Lee Waves Generated by the Passage of an Isolated Jet

MATTHEW O. G. HILLS AND DALE R. DURRAN

Department of Atmospheric Sciences, University of Washington, Seattle, Washington

(Manuscript received 10 February 2012, in final form 10 May 2012)

ABSTRACT

The behavior of nonstationary trapped lee waves in a nonsteady background flow is studied using idealized three-dimensional (3D) numerical simulations. Trapped waves are forced by the passage of an isolated, synoptic-scale barotropic jet over a mountain ridge of finite length. Trapped waves generated within this environment differ significantly in their behavior compared with waves in the more commonly studied two-dimensional (2D) steady flow. After the peak zonal flow has crossed the terrain, two disparate regions form within the mature wave train: 1) upwind of the jet maximum, trapped waves increase their wavelength and tend to untrap and decay, whereas 2) downwind of the jet maximum, wavelengths shorten and waves remain trapped. Waves start to untrap approximately 100 km downwind of the ridge top, and the region of untrapping expands downwind with time as the jet progresses, while waves downstream of the jet maximum persist. Wentzel–Kramers–Brillouin (WKB) ray tracing shows that spatial gradients in the mean flow are the key factor responsible for these behaviors. An example of real-world waves evolving similarly to the modeled waves is presented.

As expected, trapped waves forced by steady 2D and horizontally uniform unsteady 3D flows decay downstream because of leakage of wave energy into the stratosphere. Surprisingly, the downstream decay of lee waves is inhibited by the presence of a stratosphere in the isolated-jet simulations. Also unexpected is that the initial trapped wavelength increases quasi-linearly throughout the event, despite the large-scale forcing at the ridge crest being symmetric in time about the midpoint of the isolated-jet simulation.

1. Introduction

Trapped lee waves develop when air flows over a mountain under appropriate atmospheric conditions. These waves are significant because they are associated with momentum fluxes that can produce a drag on the large-scale flow (Bretherton 1969; Durran 1995; Broad 2002). Strong trapped waves can also contribute to the formation of rotors and dangerous clear-air turbulence (Doyle and Durran 2002).

Beginning with Scorer (1949), trapped lee waves have been the subject of considerable theoretical study, most of which assumed steady horizontally uniform environmental forcing. Nevertheless, observational evidence readily demonstrates that trapped waves display notable nonstationary behavior (Vergeiner and Lilly 1970; Ralph et al. 1992; Worthington and Thomas 1996), with significant changes sometimes occurring on time scales of less than 1 h (Ralph et al. 1997). Temporal changes in amplitude (Starr and Browning 1972; Brown 1983), downstream position and extent (Lindsay 1962), and horizontal wavelength (Holmboe and Klieforth 1957; Queney et al. 1960; Smith 1976; Mitchell et al. 1990; Ralph et al. 1997) have all been observed. In particular, in an analysis of 24 observed events, Ralph et al. (1997) found that the resonant wavelength of trapped waves gradually increased at an average rate of 9% h^{-1}.

Some studies focused on trapped wave transients assume steady large-scale forcing (Wurtele 1955; Nance and Durran 1998; Wurtele et al. 1999), although the lifetime of trapped wave events, which ranges from a few hours to a few days, is enough time for nonnegligible changes to occur in the background large-scale flow. Ralph et al. (1997) and Vosper and Worthington (2002) both compared model results with observations and concluded that the evolving trapped wave field can be well approximated as the response to a sequence of independent steady states. Nevertheless, Vosper and Worthington (2002) did obtain somewhat different, although not clearly better, results by switching the forcing from a series of steady states to continuously updated upstream conditions. Nance and Durran (1997) simulated several trapped wave cases in which a horizontally uniform

Corresponding author address: Matt Hills, Dept. of Atmospheric Sciences, University of Washington, Box 351640, Seattle, WA 98195.
E-mail: matthills@atmos.washington.edu

DOI: 10.1175/JAS-D-12-047.1

background wind speed gradually transitioned between two steady values; they found that complicated wave patterns could occur if waves generated after the transition overtook those generated before the transition. Lott and Teitelbaum (1993a,b) studied the response of vertically propagating mountain waves to an initial-value problem in which a horizontally uniform background flow sinusoidally accelerated from rest and then decelerated back to a resting state. The horizontal and temporal variations in the large-scale flow were coupled in a dynamically consistent manner by Chen et al. (2005, 2007), who investigated the behavior of vertically propagating waves triggered by the passage of an isolated jet over an isolated ridge. We are not aware of previous studies that investigated trapped lee waves generated by a simple idealized large-scale flow that varies in both time and space.

In this paper we examine nonstationary trapped lee waves produced by a large-scale flow similar to the isolated barotropic jet employed by Chen et al. (2005, 2007). In contrast to the single layer of uniform static stability used by Chen et al. (2005, 2007), however, we will simulate cases with vertically layered static stability structures capable of supporting trapped waves. As will be detailed later, the horizontal variations in the wind speed associated with the isolated jet turn out to exert an even more profound impact on trapped waves than they did in the vertically propagating case considered in Chen et al. (2005).

The remainder of this paper is organized as follows. Section 2 contains a description of the model used in our study and the setup of the experiment. The structure of lee waves in the isolated-jet case is discussed in section 3, followed by a quantitative analysis of the wave train using Wentzel–Kramers–Brillouin (WKB) ray tracing in section 4. Section 5 further illustrates the impact of spatial variations in the background flow on trapped waves. We consider the temporal changes in the initial trapped wave wavelength in section 6. The influence of the stratosphere on the trapped waves is discussed in section 7. A brief comparison of our idealized results with a real-world event is presented in section 8, and section 9 contains the conclusions.

2. Model description and experiment setup

The fully nonlinear, nonhydrostatic, three-dimensional numerical model used throughout this study is an updated version of the model of Durran and Klemp (1983), more recently used by Epifanio and Durran (2001) and Chen et al. (2005, 2007). To simplify the model's governing equations, we use the compressible Boussinesq and *f*-plane approximations. Terrain-following vertical coordinates are used. A split time-step scheme is employed, with the terms supporting rapid sound wave propagation integrated separately from the remaining dynamics using a smaller time step $\Delta\tau$. The model solves the following governing equations:

$$\frac{D\mathbf{v}}{Dt} + f\mathbf{k}\times\mathbf{v} + \nabla P = g\left(\frac{\theta - \theta_r}{\theta_0}\right)\mathbf{k} - \nabla\cdot\mathbf{T}, \quad (1)$$

$$\frac{D\theta}{Dt} = \nabla\cdot\mathbf{H}, \quad (2)$$

$$\frac{\partial P}{\partial t} + u_0\frac{\partial P}{\partial x} + c_{s_0}^2\nabla\cdot\mathbf{v} = 0, \quad (3)$$

where

$$\frac{D}{Dt} = \frac{\partial}{\partial t} + (u_0 + u)\frac{\partial}{\partial x} + v\frac{\partial}{\partial y} + w\frac{\partial}{\partial z}.$$

In these equations, $\mathbf{v} = (u, v, w)$ are the perturbation flow components [about a reference state of $(u_0, 0, 0)$] in the directions (x, y, z) respectively, and $\mathbf{k}$ is the vertical unit vector. A constant uniform background westerly flow u_0 is forced by a geostrophically balanced uniform north–south pressure field $-fu_0y$ (note that there is no vertical shear in the background reference state), P is the Boussinesq pressure perturbation about that mean pressure field, θ is potential temperature (θ_0 is the constant reference value of the potential temperature = 280 K), f is the Coriolis parameter (set to a constant 10^{-4} s^{-1}), and c_{s_0} is the speed of sound (specified as 300 m s^{-1}). Also, $\mathbf{T}$ and $\mathbf{H}$ are the turbulent subgrid-scale fluxes of momentum and heat, parameterized according to Lilly (1962).

The Boussinesq pressure is defined in terms of the Exner function, $\pi = (p/p_0)^{R/c_p}$, where p is pressure, p_0 is the reference surface pressure, c_p is the specific heat of air at constant pressure, and R is the gas constant. The total π is split into three component pieces: a vertically varying background reference state π_r, a north–south varying background state π_g, and the remaining perturbation π', such that $\pi = \pi_r(z) + \pi_g(y) + \pi'(x, y, z, t)$. Since there is no vertical shear in the background westerly flow, the corresponding decomposition of θ simplifies to $\theta = \theta_r(z) + \theta'(x, y, z, t)$, where the reference state is in hydrostatic balance

$$c_p\theta_r\frac{\partial\pi_r}{\partial z} = -g. \quad (4)$$

With the terms defined in this way, we can write the perturbation Boussinesq pressure field as $P = c_p\theta_0\pi'$ (Durran 2010, p. 24).

As in Chen et al. (2005, 2007), the dynamically consistent, synoptic-scale background flow is an isolated jet formed by combining u_0 with a barotropic square wave. The initial velocities $\mathbf{v}_s = (u_s, v_s, 0)$ define the square wave, where

$$u_s(x, y, z) = u_0 \cos\left[\frac{2\pi(x - x_0)}{L}\right] \cos\left(\frac{2\pi y}{L}\right), \quad (5)$$

$$v_s(x, y, z) = u_0 \sin\left[\frac{2\pi(x - x_0)}{L}\right] \sin\left(\frac{2\pi y}{L}\right), \quad (6)$$

which are nonlinearly balanced by a perturbation pressure P_s satisfying

$$\nabla \cdot [(\mathbf{v}_s \cdot \nabla)\mathbf{v}_s + f\mathbf{k} \times \mathbf{v}_s] + \nabla^2 P_s = 0, \quad (7)$$

where $L = 1200$ km, $x_0 = 150$ km, and $u_0 = 10$ m s^{-1}, giving the background flow a period τ of 33.3 h. This barotropic wave is an exact numerical solution of the governing equations and, in the absence of any topography, it would translate around the domain at a speed u_0. Thus the large-scale flow is defined by

$$\overline{u} = u_0 + u_s(x - u_0 t, y, t), \quad \overline{v} = v_s(x - u_0 t, y, t),$$
$$\overline{w} = 0, \quad \overline{P} = P_s(x - u_0 t, y, t).$$

With this large-scale flow, winds at the center of the mountain vary as

$$U(t) = u_0\left[1 - \cos\left(\frac{2\pi t}{\tau}\right)\right]. \quad (8)$$

Figure 1 shows the large-scale flow at the initial time and the location of the terrain. The mountain is centered at $(x, y) = (x_0, L/2)$, in a region of initially stagnant flow,

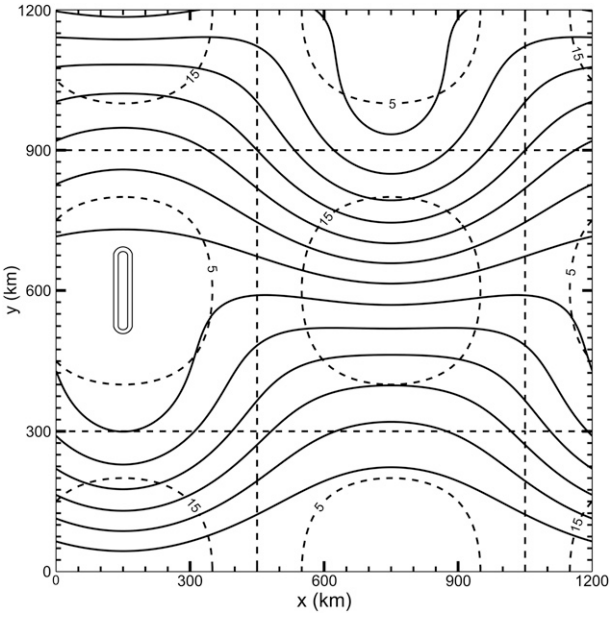

FIG. 1. Contours of zonal wind speed (dashed lines; contours are 5, 10, and 15 m s^{-1}), and isobars of pressure ($\overline{P} - fu_0 y$; solid lines, low pressure at top), for the initial synoptic-scale background flow. Terrain is shown by thin elongated contours at elevations of 100 and 200 m.

to minimize any initial transients. The terrain used is a uniform ridge of finite length, with the same parametric dependence considered by Epifanio and Durran (2001) and Chen et al. (2005, 2007):

$$h_s(x, y) = \begin{cases} \dfrac{h}{16}\left[1 + \cos\left(\dfrac{\pi r}{4a}\right)\right]^4, & \text{if} \quad r \le 4a; \\ 0, & \text{otherwise,} \end{cases} \quad (9)$$

where

$$r^2 = \begin{cases} (x - x_0)^2 + [|y - L/2| - (\beta - 1)a]^2, & \text{if} \quad |y - L/2| > (\beta - 1)a; \\ (x - x_0)^2, & \text{otherwise,} \end{cases} \quad (10)$$

where the approximate half-width at half height is $a = 18$ km, and the mountain has an aspect ratio of 5. A mountain height of $h = 250$ m is used.

We use a large time step of $\Delta t = 12$ s, with a small time step of $\Delta\tau = 1$ s. The horizontal domain is 1200×1200 km^2, with $\Delta x = \Delta y = 1$ km, and we use doubly periodic boundary conditions with a free-slip lower boundary. The depth of the physical domain is 36 km, with a vertical resolution of $\Delta z = 200$ m for $z < 10$ km, which is gradually stretched to $\Delta z = 500$ m across $10 < z < 15$ km, where it remains until the rigid-lid upper boundary at $z = 36$ km. To prevent spurious wave reflections off of this upper boundary, a damping layer lies across $20 < z < 36$ km. We use the scale-selective Rayleigh damping layer described by Chen et al. (2005), in which the terms

$$-\nu(z)(\mathbf{v} - \mathbf{v}_l) \quad \text{and} \quad -\nu(z)(\theta - \theta_l)$$

are added to the right-hand sides of (1) and (2), respectively. The large-scale horizontal velocities toward which the solution is damped are computed by Fourier

transforming u and v at every level within the sponge layer at each large time step, discarding all components with wavelengths shorter than $L/4 = 300$ km, and inverse transforming. The large-scale values for the vertical velocity w_l and the potential temperature θ_l are set to zero for consistency with the rigid-lid condition. The value of the Rayleigh damping coefficient ν is zero below the sponge layer and increases with height within the layer, following (29) of Durran and Klemp (1983) to a maximum of $\alpha = 5 \times 10^{-3}$ s^{-1}.

Additional three-dimensional simulations have been computed using a spatially uniform, time-varying background flow, in which the y extent of the domain is reduced to 400 km for computational efficiency, and open boundary conditions are imposed at the north and south boundaries. The mean flow varies everywhere with the same profile as at the ridge center in the isolated-jet simulation, described by (8); this is achieved by artificially forcing the large-scale flow. The vertical structure remains the same as in the full 3D simulations, except the Rayleigh damping layer is removed and replaced with the KDB radiation condition at the upper boundary (Bougeault 1983; Klemp and Durran 1983). The terrain and all other numerical parameters in these simulations are identical to those in the isolated-jet case.

The mountain lee waves are trapped, or partially trapped, by changes in static stability with height, such that

$$N = \begin{cases} N_l = 0.0118\,\text{s}^{-1}, & \text{for} \quad z < 3\,\text{km}, \\ N_u = 0.003\,\text{s}^{-1}, & \text{for} \quad 3 < z < 12\,\text{km}, \\ N_s, & \text{for} \quad z > 12\,\text{km}. \end{cases}$$

The values of N in the lowest two layers are chosen to generate trapped lee waves with physically realistic wavelengths that can be reasonably resolved by our 1-km horizontal grid spacing.[1] Four different values of N_s are considered, but in most of the paper we will focus on just the no-stratosphere case, $N_s = 0.003$ s^{-1} (giving a two-layer structure), and the strong-stratosphere case, $N_s = 0.02$ s^{-1}.

3. Description of the nonstationary behavior

Our analysis will focus primarily on the waves along $y = L/2$, the centerline across the mountain where the mean flow is purely in the x–z plane. The vertical velocity (color fill) and potential temperature in a central portion of this x–z cross section are shown in Fig. 2 at several times between hours 16 and 28 for the strong-stratosphere case. Since the background flow translates without perturbations, all structure in Fig. 2 is produced by the trapped waves. Also appearing in Fig. 2 are isotachs of the large-scale horizontal velocity $\overline{u}$ (vertical lines), which attains a maximum value of 20 m s^{-1} (thick black line).

The cross-mountain flow becomes strong enough to force trapped waves in the model at approximately hour 12. Between hours 12 and 19, the wave train gradually extends downstream in a manner similar to that occurring in a flow that is instantaneously accelerated from rest and then held steady, except that in our case the wavelength is not uniform along the wave train. This similarity to an impulsively started flow ceases shortly after the large-scale jet maximum passes over the mountain. By hour 22 (Fig. 2c), the wavelength of the waves between the ridge crest and the jet max (the location of the thick black 20 m s^{-1} contour) has increased considerably, and some waves have begun to develop upstream phase speeds. The third and fourth trapped waves (in the region $250 \le x \le 320$ km) have also become much weaker. As the large-scale jet maximum continues to translate downstream, the first two waves in the lee of the mountain are largely maintained, but all other lee waves overtaken by the jet maximum begin to experience an increase in their wavelength and decay (Figs. 2c–e). In contrast, waves downstream of the jet maximum experience a decrease in wavelength and almost no loss of amplitude. By hour 28, the only trapped waves that remain are those which are either still downstream of the jet maximum or were only recently overtaken by that jet.

Figure 3 shows contours of the wave-induced perturbation zonal velocity field u' (i.e., the zonal velocity that remains after subtracting the instantaneous value of $\overline{u}$). Between hours 19 and 24, u' amplitudes at low levels in trapped waves 3 and 4 decay significantly, while the u' values in the upper troposphere and lower stratosphere are maintained or slightly increase.[2] The increase in wavelength and the shift in wave amplitude toward higher levels suggests that these waves are becoming untrapped.

The presence of a stratosphere has surprisingly little influence on the structure (wavelength and location) and evolution (growth and decay) of these nonstationary trapped waves (changes in amplitude do occur, however, with weaker waves in the no-stratosphere case, as discussed in section 7). Vertical cross sections of w, θ, and $\overline{u}$ along the

[1] Vertical wind shear also plays an important role in trapping most atmospheric lee waves and the influence of such shear will be pursued in future research.

[2] The increase in wave activity aloft is more pronounced for the perturbation zonal flow as u' increases more strongly with an increase in stability than w.

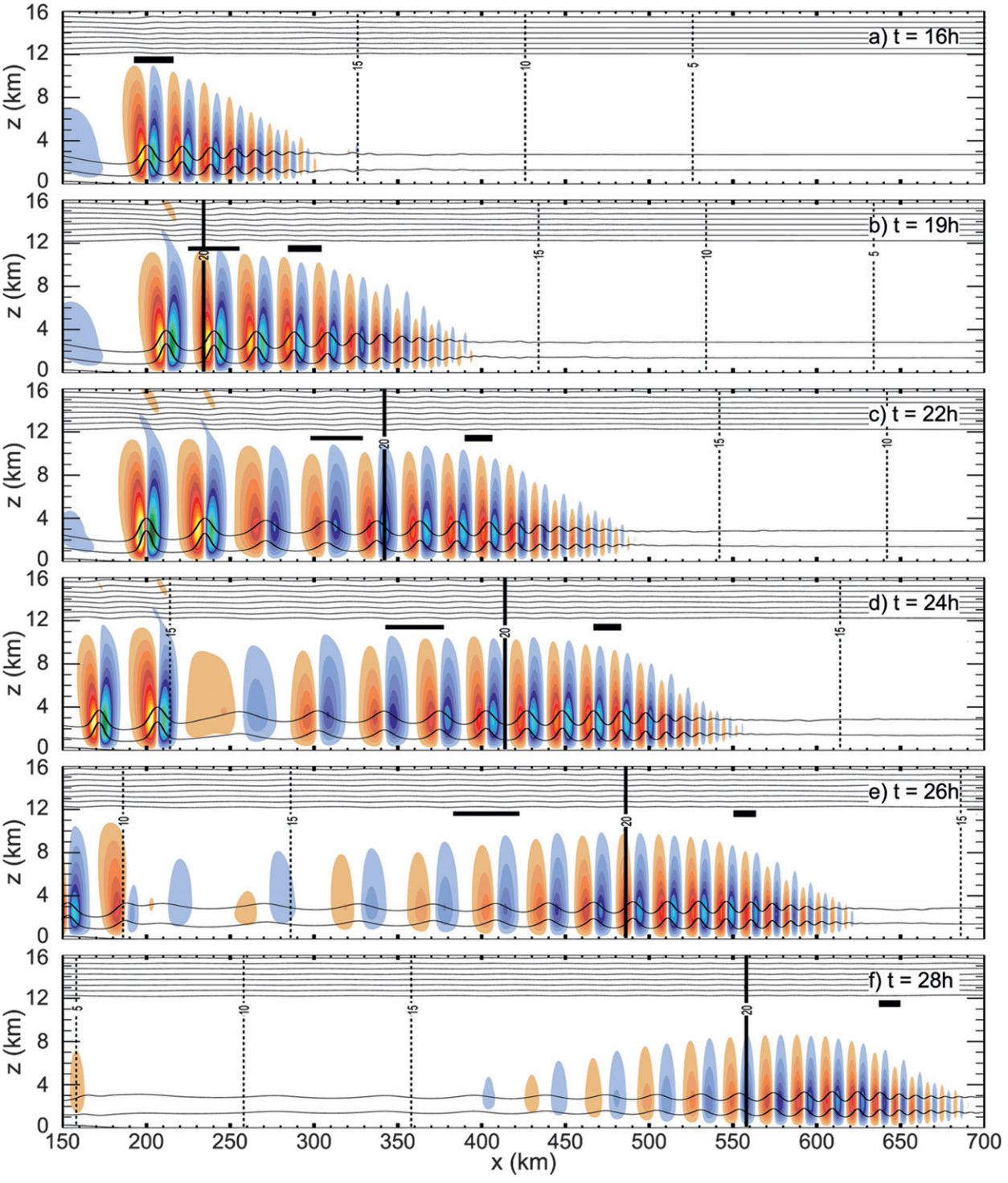

FIG. 2. Vertical cross sections for the strong-stratosphere case along $y = L/2$ of vertical velocity (color fill with contour interval = 0.4 m s^{-1}; white fill for $-0.4 < w < 0.4$ m s^{-1}), and potential temperature (thin horizontal isentropes; contour interval = 6 K), at times (a) 16, (b) 19, (c) 22, (d) 24, (e) 26, and (f) 28 h. Also shown is the large-scale zonal velocity (thick dashed vertical isotachs; contour interval = 5 m s^{-1}). Horizontal thick (thin) black lines at $z = 11.5$ km show the location and wavelengths of waves launched at hour 16 (18), whose properties are given in Table 1.

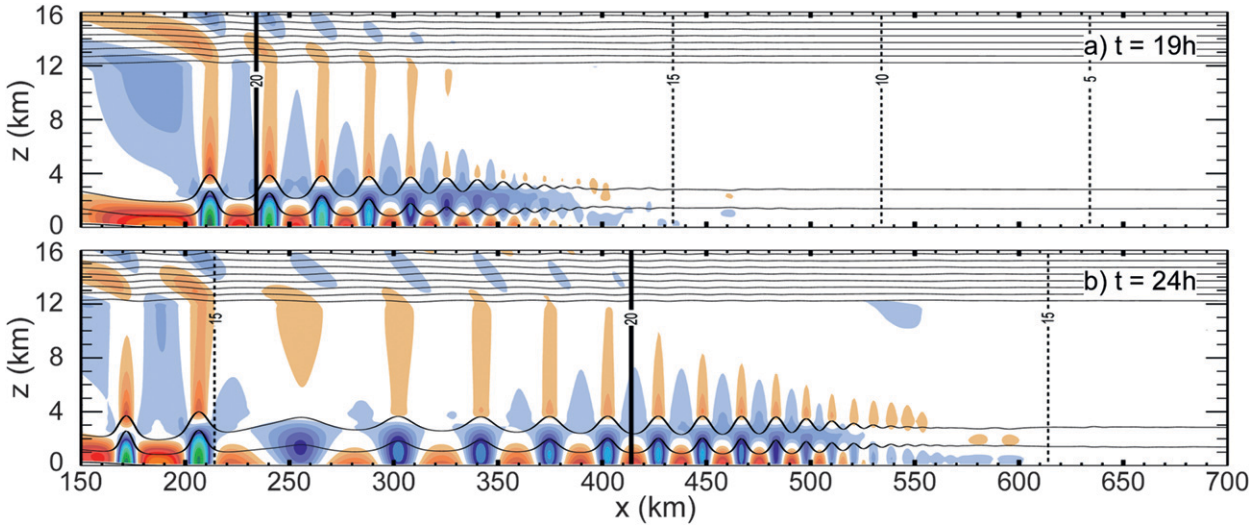

FIG. 3. As in Fig. 2, but with the perturbation zonal velocity (color fill with contour interval = 1 m s^{-1}; white fill for $-1 < u' < 1$ m s^{-1}), at times (a) 19 and (b) 24 h.

cross-mountain centerline for the no-stratosphere case are shown in Fig. 4. A comparison of Figs. 2 and 4 shows that the overall evolution of the wave train is essentially unchanged by the addition of a stratosphere.

While our WKB analysis in the following section treats waves along the centerline as if they were strictly two-dimensional, in practice north–south variations occur in the wave train because of the simulations being 3D. The evolution of the wave train in the x–y plane is shown by contours of w at $z = 3$ km for the no-stratosphere case in Fig. 5. Also shown in Fig. 5 are a few velocity vectors for the large-scale flow $(\overline{u}, \overline{v})$. Along $y = 600$ km, the wave

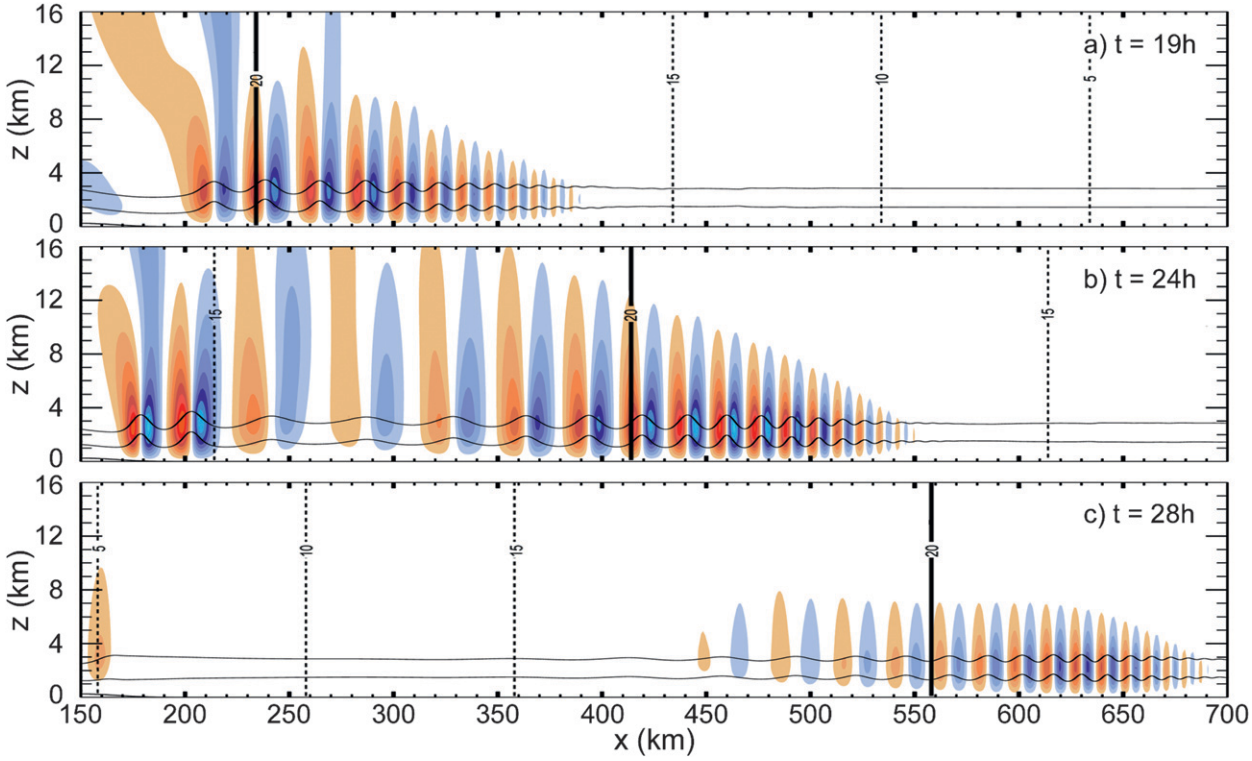

FIG. 4. As in Fig. 2, but for the no-stratosphere case, at times (a) 19, (b) 24, and (c) 28 h.

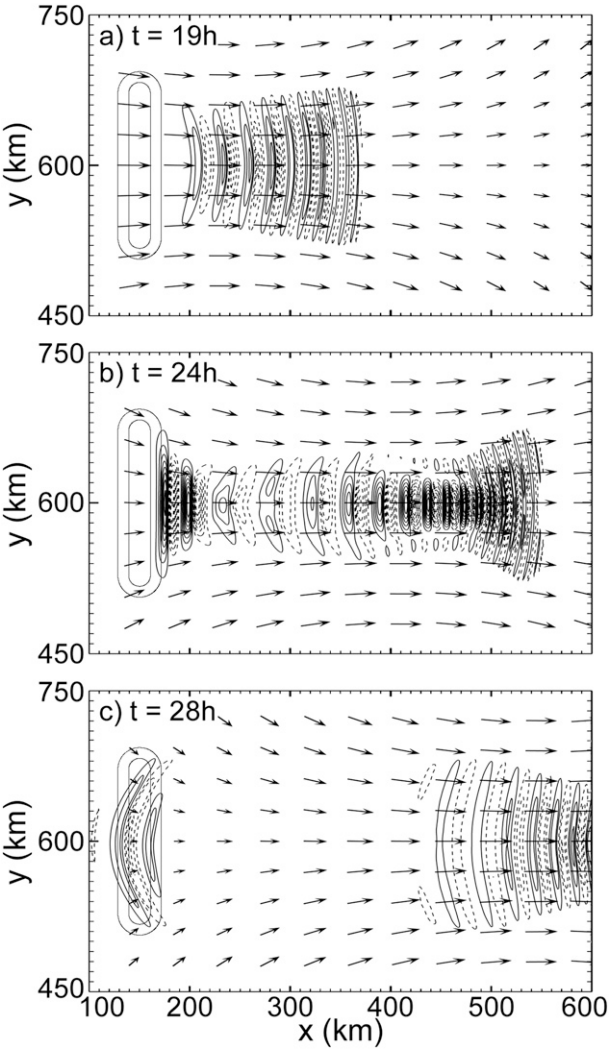

FIG. 5. Horizontal cross sections of vertical velocity for the no-stratosphere case at $z = 3$ km, for times (a) 19, (b) 24, and (c) 28 h. Solid (dashed) contours show ascent (descent); in (a) contour interval = 0.8 m s^{-1}, in (b) and (c) contour interval = 0.4 m s^{-1}. Vectors show the large-scale horizontal flow. Terrain is shown by thin elongated contours at elevations of 100 and 200 m.

structure is indeed quasi-two-dimensional at each time. However, three-dimensional behavior occurs away from the centerline as a result of a combination of two main processes. First, as shown by the velocity vectors in Fig. 5, the large-scale flow converges (diverges) upwind (downwind) of the jet axis, and this pattern tends to advect the wave structure. Second, the waves are forced by a finite-length ridge, which affects their downstream evolution as discussed by Sharman and Wurtele (2004). At hour 19, the meridional structure of the wave train in the region $200 \le x \le 370$ km is controlled by advection by the large-scale flow—with an upstream tilt at the northern and southern ends of the w contours. Figure 5b shows that at hour 24, this advection by the large-scale flow is still dominant downwind of the jet axis ($x = 414$ km). In the region $210 \le x \le 380$ km, however, the northern and southern ends of the w contours tilt downstream and the maximum amplitudes shift north and south of the centerline. The wave pattern in this region is similar to that for trapped waves in a horizontally uniform flow forced by a long, but finite, ridge (Sharman and Wurtele 2004). By hour 28, the loss of wave activity in the region $200 \le x \le 420$ km and $520 \le y \le 680$ km is illustrated, and the remaining waves in the region $420 \le x \le 600$ km experience a downwind tilt at their north–south edges typical of waves forced by a finite ridge.

4. WKB analysis

A basic understanding of the structure and evolution of the waves in the preceding simulations may be obtained through WKB ray tracing, analyzing waves in the x–z cross section along the cross-mountain centerline as if they were purely two-dimensional. Trapped waves propagate horizontally, with a horizontal structure along this centerline of the form $e^{i(kx-\omega t)}$, where k is the wavenumber and ω is the frequency. Because of the x–t dependence of the large-scale flow along the centerline, ω is a function of k, x, and t. The general ray-tracing equations applicable to such waves are (Whitham 1974; Bühler 2009)

$$\frac{D_g k}{Dt} = -\left.\frac{\partial \omega}{\partial x}\right|_{k,t}, \tag{11}$$

$$\frac{D_g \omega}{Dt} = \left.\frac{\partial \omega}{\partial t}\right|_{k,x}, \tag{12}$$

where

$$\frac{D_g}{Dt} = \frac{\partial}{\partial t} + c_g \frac{\partial}{\partial x}$$

is the rate of change moving through the fluid at the group velocity $c_g = \partial\omega/\partial k$.

Consider the no-stratosphere case, in which the Brunt–Väisälä frequencies in the upper and lower layers are N_u and N_l, respectively. Let the horizontal phase speed be $c = \omega/k$ and define the intrinsic frequency as

$$\tilde{\omega} = (c - \overline{u})k. \tag{13}$$

Assuming the vertically uniform large-scale $\overline{u}$ varies slowly in x and t, a necessary condition for a given wave to be trapped is that $N_u < |\tilde{\omega}| < N_l$. As noted by Nance and Durran (1997), nonstationary trapped waves in such two-layer atmospheres satisfy the dispersion relation

$$\cot(S_l d) = -\frac{S_u}{S_l}, \tag{14}$$

where d is the depth of the lower layer,

$$S_l = \left[\frac{N_l^2}{(c - \overline{u})^2} - k^2\right]^{1/2} \quad \text{and} \quad S_u = \left[k^2 - \frac{N_u^2}{(c - \overline{u})^2}\right]^{1/2}. \tag{15}$$

For nonstationary trapped waves described by the dispersion relation in (14) with $\overline{u}$ a slowly varying function of x and t, the WKB ray-tracing equations in (11) and (12) become

$$\frac{D_g k}{Dt} = -k\frac{\partial \overline{u}}{\partial x}, \tag{16}$$

$$\frac{D_g \omega}{Dt} = k\frac{\partial \overline{u}}{\partial t}. \tag{17}$$

The group velocity required for the evaluation of D_g/Dt is

$$c_g = \overline{u} + \frac{S_l^4 S_u d(c - \overline{u})^3}{N_l^2 S_l^2 S_u d + k_l^2(N_l^2 - N_u^2)\sin^2(S_l d)}, \tag{18}$$

which, recalling that $\omega = ck$, may be determined from (14) and (15).

Large-amplitude trapped lee waves are first generated in the model after approximately hour 12. Once they are launched, the behavior of individual wave packets were calculated and traced along their ray paths until they either became untrapped [the dispersion relation (14) is only valid for trapped waves] or until the end of the simulation, whichever occurred sooner. Packets were launched from the upwind edge of the lee wave train, which we took as the position of the first downdraft after the first updraft in the lee of the mountain. The local value of k evaluated at this point from the full model output[3] was used to compute an initial value for k from (14). Each packet was then followed downstream using only the large-scale $\overline{u}$, N_l, N_u, and (16)–(18) to update the packet's wavenumber, frequency, and location.

The downstream evolution of the trapped wave wavelengths predicted by the ray-tracing analysis and measured from the numerical simulations are compared in Table 1 (the locations of these wave packets are illustrated in Fig. 2). The packet launched at hour 16 persists throughout the simulation, while the packet launched at hour 18 ultimately decays. There is very good agreement between the wavelengths predicted via ray tracing and those measured directly from the no-stratosphere case; the errors are less than approximately 5%. Good quantitative agreement is also obtained for the strong-stratosphere case, with errors no larger than about 7%. This strong agreement between the two-layer analytic model and the three-layer, strong-stratosphere simulation may be surprising, but it is consistent with the previously noted similarity of the trapped wave behaviors in the no-stratosphere and strong-stratosphere cases. Thus, despite the various approximations associated with the use of a linear 2D WKB analysis, we are confident in the accuracy of our ray-tracing scheme. The following discussion will focus on the strong-stratosphere case because this represents the more realistic situation. The same analyses have, however, been performed for the no-stratosphere case, and the same conclusions are reached for both cases.

TABLE 1. Comparison of wavelengths predicted by the ray-tracing scheme and the measured values from the numerical simulations.

Time (h)	Ray-tracing λ (km)	No-stratosphere model λ (km)	Strong-stratosphere model λ (km)
		Launched at hour 16	
16	23.8	23.5	24.6
19	19.6	19.5	20.5
22	16.9	17.4	18.0
25	13.9	14.7	14.5
28	11.4	11.4	11.4
		Launched at hour 18	
18	30.7	29.4	30.1
20	30.4	29.6	29.2
22	31.4	31.3	32.6
24	34.0	33.2	32.8
26	38.8	37.4	36.9

Figure 6 shows the WKB ray-tracing-predicted wavelengths of wave packets launched at hourly intervals from the upwind edge of the lee wave train during the strong-stratosphere simulation. The wavelengths of packets launched early in the simulation (hours 13–16) decrease with time, whereas the wavelengths of the packets launched at hours 19 and 20 continually increase. The packets initialized at hours 17 and 18 exhibit an intermediate behavior; they experience an initial decrease in wavelength followed by a continual increase. These changes in wavelength are consistent with those apparent in Figs. 2–4. The disparate behaviors in different sections of the wave train are associated with the position of the wave packets with respect to the jet maximum.

[3] The waves may be launched with nonzero phase speed because of a drift in the starting location of the wave train that occurs as variations in the background flow produce nonsteady waves.

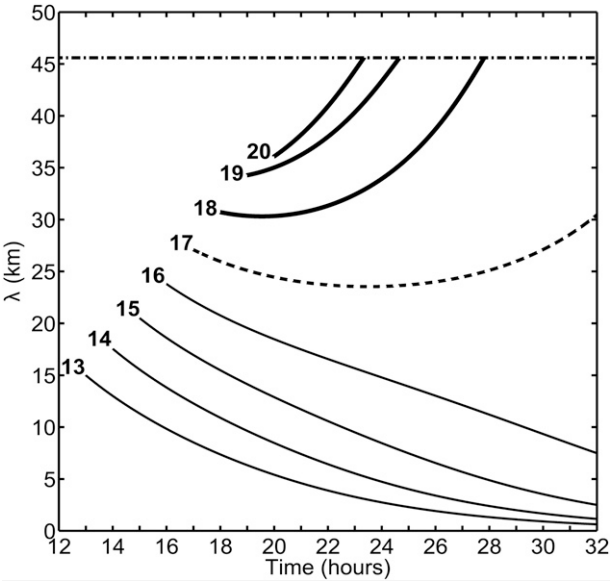

FIG. 6. Wavelength along ray paths following wave packets generated hourly between hours 13 and 20. Thin contours: packets remain trapped. Thick contours: packets untrap. Thick dashed contour: packet tends toward untrapping but remains trapped. The thin dot-dashed horizontal line marks the critical wavelength at which waves become untrapped.

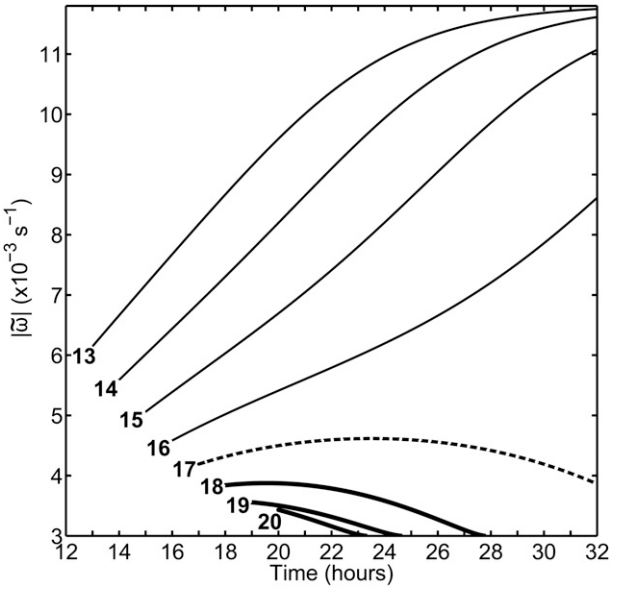

FIG. 7. As in Fig. 6, but for absolute intrinsic frequency $|\tilde{\omega}|$ ($\times 10^{-3}$ s^{-1}). Limits on the y axis represent the bounds on $|\tilde{\omega}|$ for waves to be trapped.

According to (16), the changes in wavenumber and wavelength along a ray path are determined by the spatial gradients of $\overline{u}$. Wave packets downstream of the jet max are in an environment where $\partial\overline{u}/\partial x < 0$ and consistent with (16), their wavenumber (wavelength) increases (decreases). Opposite changes in wavelength occur upstream of the jet max, where $\partial\overline{u}/\partial x > 0$.

The intrinsic frequencies computed along each ray show the same disparate behavior in different sections of the wave train. Along each ray

$$\frac{D_g\tilde{\omega}}{Dt} = \frac{D_g}{Dt}(\omega - \overline{u}k) = \frac{D_g\omega}{Dt} - \overline{u}\frac{D_gk}{Dt} - k\frac{D_g\overline{u}}{Dt}. \quad (19)$$

Defining the intrinsic group velocity $\tilde{c}_g = c_g - \overline{u}$, and using (16) and (17), the preceding may be rewritten as

$$\frac{D_g\tilde{\omega}}{Dt} = -\tilde{c}_g k\frac{\partial\overline{u}}{\partial x}. \quad (20)$$

In our waves, $k > 0$ and $\tilde{c}_g < 0$ for all wave packets; thus, as was the case for the horizontal wavelength, the sign of the $\tilde{\omega}$ tendency along different ray paths will be governed by the sign of $\partial\overline{u}/\partial x$. Figure 7 shows the values of $|\tilde{\omega}|$ along the ray paths of the same wave packets considered in Fig. 6.

The waves associated with packets launched from hour 19 onward are generated after the time of peak flow and have group velocities slower than the 10 m s^{-1} speed at which the background flow is translating. As such, they remain in an area where $\partial\overline{u}/\partial x > 0$ throughout their life and, as shown in Fig. 7, their $|\tilde{\omega}|$ continually decreases. As they fall farther behind the jet maximum, the local value of $\partial\overline{u}/\partial x$ increases, increasing the rate of change in k and $|\tilde{\omega}|$ (see Figs. 6 and 7). These packets become untrapped first, and are responsible for the loss of wave activity in the region $250 \le x \le 300$ km between hours 22 and 26 in Fig. 2.

Packets launched prior to hour 19 initially lie in a region where $\partial\overline{u}/\partial x < 0$, so, at least at the beginning of their life, their absolute intrinsic frequency increases and their wavelength decreases. The jet maximum passes through packets launched between hours 16.5 and 18, and the tendencies for λ and $|\tilde{\omega}|$ reverse once the packets find themselves in a region where $\partial\overline{u}/\partial x > 0$. It is primarily the waves generated during the period $17 \le t \le 18$ h that produce the continued downstream growth of the region of weak waves visible after hour 26 in Fig. 2. Nevertheless, not all of the packets that slip upwind of the jet maximim actually become untrapped: those packets generated between hours 16.5 and 17 are overtaken by the jet but do not have sufficient time to untrap before the end of the simulation.

On the other hand, all waves launched between hours 12.5 and 16 have group velocities faster than the translation speed of the jet maximum and remain in an environment where $\partial\overline{u}/\partial x < 0$. Their wavelength continually decreases while their $|\tilde{\omega}|$ continually increases. They do

not become untrapped and compose the bulk of the set of waves present at the end of the simulation in Fig. 2. Some of these waves do, however, develop such short wavelengths that they are damped out by the numerical smoother.

Recall that wave packets cannot be trapped unless $N_u < |\tilde{\omega}| < N_l$. The vertical axis in Fig. 7 begins at the value $|\tilde{\omega}| = 0.003\,\mathrm{s}^{-1} = N_u$, implying that the curves that intersect the bottom of the plot are associated with wave packets that become untrapped. Packets launched between hours 18 and 20 become untrapped during the simulation, and the packet launched at hour 17 would also become untrapped if there were sufficient time before the end of the simulation. In a two-layer atmosphere with constant $\overline{u}$, the resonance condition for the existence of nonstationary trapped lee waves is

$$N_l^2 - N_u^2 \geq \frac{\pi^2(\overline{u} - c)^2}{4d^2} = \left(\frac{\tilde{\omega}\lambda}{4d}\right)^2, \qquad (21)$$

where $\lambda = 2\pi/k$ is the resonant wavelength. This is a straightforward generalization of the classical resonance condition for stationary waves (Scorer 1949). Substituting N_u for $\tilde{\omega}$ in (21), we may obtain an expression for the critical wavelength at which nonstationary waves untrap:

$$\lambda_c = 4d\left(\frac{N_l^2}{N_u^2} - 1\right)^{1/2}, \qquad (22)$$

which for the two-layer structure in our ray-tracing analysis implies $\lambda_c = 45.6$ km. As shown by the thin dot-dashed contour in Fig. 6, this value is consistent with the wavelengths at which untrapping occurs.

The ground-relative phase speed of the wave packets also differs between packets forced early and those forced later, as may be computed via ray tracing (not shown) and as illustrated in Fig. 8 by the Hovmöller diagram of w at $z = 3$ km from the strong-stratosphere simulation.[4] The superimposed thick black lines in Fig. 8 indicate the paths of rays launched between hours 13 and 20. Waves launched prior to hour 17 maintain a downwind phase speed throughout the simulation, while those launched later eventually develop an upwind phase speed. Nevertheless, despite the reversal in the phase speed of some wave packets, the group velocity remains positive for all packets at all times. The increase in wavelength predicted by ray tracing is readily apparent

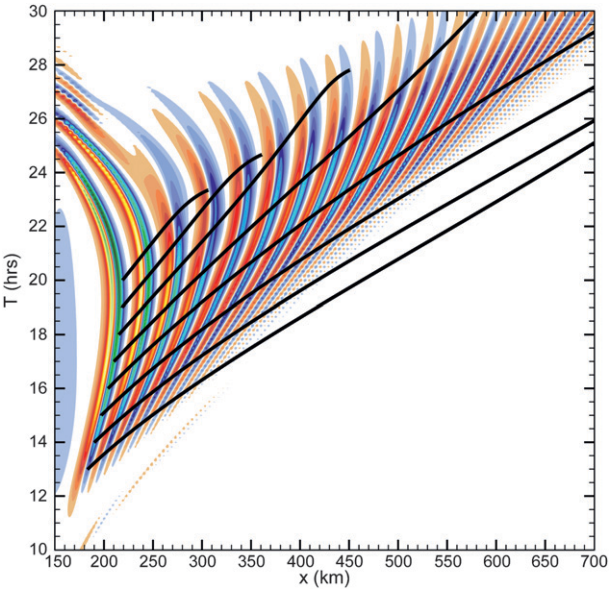

FIG. 8. Hovmöller plot of vertical velocity for the isolated-jet strong-stratosphere case at $z = 3$ km (color fill with contour interval = 0.4 m s^{-1}; white fill for $-0.4 < w < 0.4$ m s^{-1}). Solid overlaid black lines show the ray paths of wave packets generated hourly between hours 13 and 20. Lines terminate where wave untraps. The centerline of the ridge lies along the left axis.

along rays launched at hours 18–20 during the simulation, as well as by the loss in amplitude of their associated wave packets due to untrapping. The ends of rays 19 and 20, which indicate the x–t location at which packets untrap, coincide with times and locations at which the simulated waves begin to rapidly lose amplitude. Ray path 18 also terminates at a point associated with the rapid dissipation of the simulated waves. The simulated wave front appears to dissipate more rapidly along rays 13–15 than one might expect from ray tracing as these rays clearly move ahead of the leading edge of the wave train in the numerical simulation. Wave packets in this region develop wavelengths shorter than $5\Delta x$, and are eventually eliminated by the fourth-order numerical smoother. We expect such waves would be present in a sufficiently high-resolution simulation.

5. Comparison with spatially uniform unsteady flow

The preceding analysis suggests that trapped lee waves generated by the passage of an isolated jet over a ridge will evolve in a substantially different manner than those in a ''uniform-unsteady'' case in which the large-scale velocity throughout the domain varies in the same manner as the large-scale velocity at the center of the mountain in the isolated-jet case. To test this, we conducted a 3D uniform-unsteady simulation using

[4] The stippled pattern along the leading edge of the waves in Fig. 8 is generated by the plotting software interpolating coarsely resolved data; 1-km horizontal resolution data are archived only every 10 min because of memory constraints.

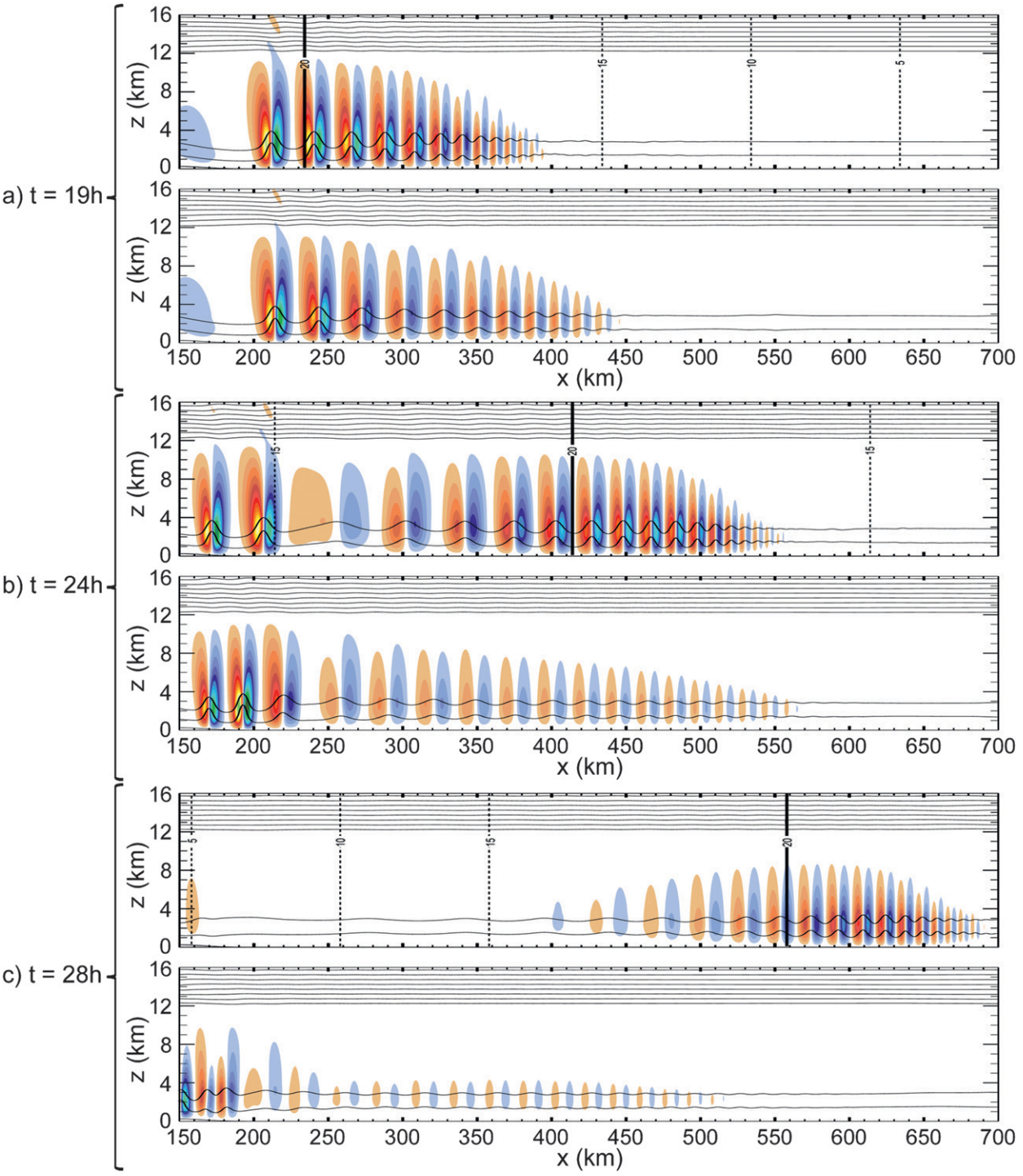

FIG. 9. As in Fig. 2, but comparing (top) the isolated-jet and (bottom) the uniform-unsteady wave trains at times (a) 19, (b) 24, and (c) 28 h.

the strong-stratosphere stability profile (as described in section 2).

Figure 9 compares w and θ along the centerline at three different times in the isolated-jet and uniform-unsteady cases. The initial development of the wave train is similar in both cases; at hour 19 (Fig. 9a) the main difference is at the leading edge of the wave train. In the region $350 \leq x \leq 400$ km, the wavelength in the isolated-jet case has been reduced to roughly half of the corresponding value in the uniform-unsteady case because

$\partial\overline{u}/\partial x < 0$ in this region of the isolated jet. As a consequence of this reduction in wavelength, the waves at the leading edge of the isolated-jet wave train are damped by the fourth-order horizontal smoother. Conversely, in the uniform-unsteady case there is no temporal change in wavelength within individual wave packets because $\partial\overline{u}/\partial x = 0$. Nevertheless, those packets launched earlier have shorter wavelengths than those launched later because they were forced with a shorter resonant wavelength due to the weaker $\overline{u}$ when these packets were generated.

By hour 24 (Fig. 9b) the two cases look very different. There are no changes in wavelength or any tendency for wave untrapping in the uniform-unsteady case, but the amplitude of the downstream waves has been gradually reduced by lateral dispersion and the fourth-order numerical smoother. In contrast, in the isolated-jet case, the waves in the region between $x = 200$ km and the location of the jet axis (coincident with the 20 m s^{-1} isotach) have begun to increase their wavelength and are tending toward untrapping. Also of interest are the waves just downstream of the jet maximum, which have become much stronger than those in the same location in the uniform-unsteady case. The amplification of these waves, which will be the subject of a subsequent paper, is due to the conservation of wave action and to lateral transport of wave activity in the large-scale square-wave pattern.

At hour 28, the deceleration of the mean flow has reversed the phase speed in the entire wave train in the uniform-unsteady case, and all waves are shifting back toward the mountain (Fig. 9c). These waves remain trapped but continue to lose amplitude due to lateral dispersion and numerical dissipation. The isolated-jet case looks completely different: a 250-km-wide region downstream of the mountain crest is almost wave-free, while a group of relatively large-amplitude trapped waves are maintained downstream of the jet maximum.

The behavior of the wave train in the uniform-unsteady case may also be analyzed using WKB ray tracing. As implied by (16) and (20), in this case the wavelength and intrinsic frequency within individual wave packets remain constant. Thus changes in the phase speeds and group velocities of individual wave packets arise entirely due to temporal variation in $\overline{u}$. Since $\overline{u}$ varies sinusoidally in time, both the phase lines and the ray paths must lie along sinusoidal curves in the x–t plane. As shown by the Hovmöller diagram of w at $z = 3$ km in Fig. 10, this is indeed the case. In marked contrast to the corresponding result for the isolated-jet case (Fig. 8), Fig. 10 clearly shows a symmetric reversal in wave packet motion in the uniform-unsteady case.

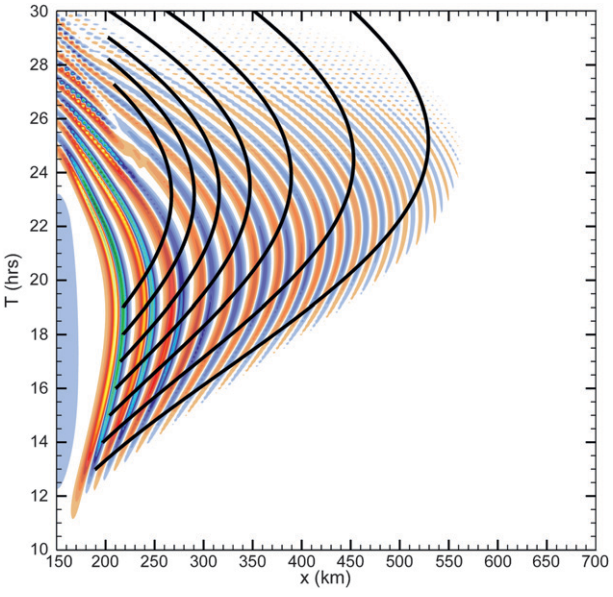

FIG. 10. As in Fig. 8, but for the uniform-unsteady strong-stratosphere simulation. Lines terminate where packet begins to move over the terrain.

6. Lengthening of the initial lee wave wavelength

Observations detailing changes in the lee-wave wavelength have focused primarily on the region close to the terrain, where the waves have the largest amplitude. In the absence of other factors, the sinusoidal temporal variation in the large-scale cross-mountain flow will tend to force trapped waves whose initial resonant wavelength varies symmetrically about the time of maximum wind (hour 16.5). However, as shown in Fig. 6, that is not the case in these simulations. Instead the initial wavelength of trapped waves in both the isolated-jet and the uniform-unsteady cases gradually increases during the entire period that trapped waves are generated. The wavelength at which the trapped lee waves are initially triggered in the isolated-jet case increases almost linearly between hours 12.5 and 19.5 at approximately 3.2 km h^{-1} (Fig. 11a). A similar, though less strictly linear, increase occurs in the uniform-unsteady case (Fig. 11b). These are equivalent to increases of 11%–12% h^{-1} with respect to the average wavelength over the entire period, which is close to the 9% h^{-1} estimated by Ralph et al. (1997) as the average rate at which the wavelength increased in a set of 24 observed nonstationary lee-wave events. Ralph et al. (1997) suggested that this increase is due to diurnal heating modifying the static-stability profile in a way that increases the resonant wavelength. While diurnal heating may indeed be the mechanism underlying the changes in those observed cases, there is no diurnal heating in these simulations.

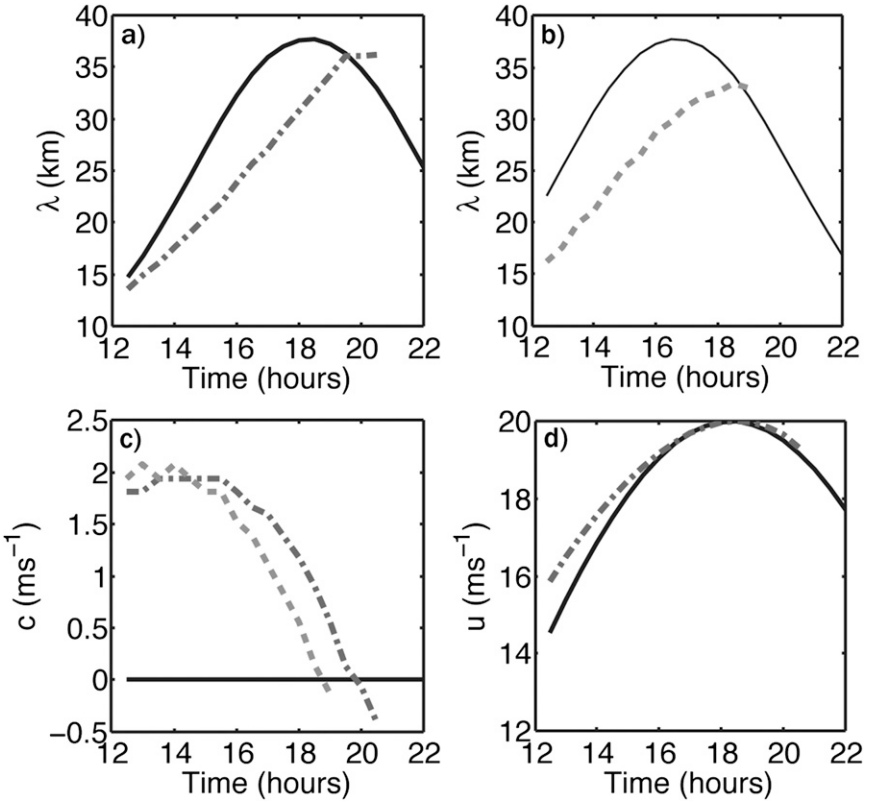

FIG. 11. Initial lee-wave wavelength as a function of time in (a) the isolated-jet (dot-dashed) and (b) the uniform-unsteady (dashed) cases. In both panels the solid line shows the resonant wavelength forced by the large-scale flow at the fixed average downstream location from which the waves are launched. (c) Phase speed at which the waves are launched. (d) Comparison of large-scale wind speed at the actual (dot-dashed) and average (solid) launch points in the isolated-jet case.

Also plotted in Fig. 11a is the resonant wavelength for a stationary initial lee wave forced by the large-scale flow at the average location of the upwind edge of the trapped wave train[5] (about 60 km downstream of the ridge crest). The extent to which the large-scale wind at this average location provides a good estimate of the actual large-scale wind at the drifting position of the leading edge of the wave train is shown in Fig. 11d, which indicates that the fixed-point estimate is good over most of the period; the largest errors (2 m s^{-1}) occur at hour 12.5. Information similar to that in Fig. 11a is displayed for the uniform-unsteady case in Fig. 11b, although since the large-scale wind speed is uniform throughout the domain, in this case the longest stationary wavelength occurs at the time of peak wind, hour 16.5.

Except for the time when the waves are first triggered (hour 12.5), the wavelength predicted for a stationary initial lee wave forced by the large-scale winds in the isolated-jet case does not match the actual wavelength at which the waves form (Fig. 11a). Furthermore, in contrast to the behavior suggested by the stationary-forcing-location large-scale resonance condition, the wavelength of the waves that actually form never starts decreasing; instead, new waves simply stop forming after hour 20.5. Roughly similar behavior is present in the case with the uniform-unsteady large-scale flow (Fig. 11b). The stationary resonance condition gives a poor prediction of the actual trapped wavelength because the waves are triggered by the downstream edge of a hydrostatic mountain wave that is propagating downwind until about hour 19. It is therefore necessary to predict the initial resonant wavelength using the correct value of c in (14). The phase speeds at which waves are triggered in the isolated-jet and uniform-unsteady cases are plotted in Fig. 11c. In both cases the waves are first triggered while moving downstream at about 2 m s^{-1}. This phase speed eventually drops to zero around hour 19, and then

[5] Recall that this point is taken to be the location of the first downdraft after the first updraft in the lee of the mountain—a location that moves with time (cf. initial wave location in Figs. 2a–c). It takes nearly 2 h for the jet maximum to travel between the crest and this location.

the generation of new trapped waves ceases shortly after the phase speed reverses sign.

The downstream phase speed at which the waves are triggered in these simulations may be exaggerated because of the lack of surface friction in the numerical model (Richard et al. 1989). Nevertheless, the key reason that there is no period during the simulation when the initial trapped wavelengths are decreasing is that wave generation stops when the initial-wave phase speed becomes negative. Examination of satellite photos suggests a tendency for the waves to begin a similar upstream shift near the end of some trapped wave events, and we are continuing to study the prevalence and importance of this behavior.

7. Influence of a stratosphere on trapped waves

The preceding simulations have revealed two interesting aspects of the influence of the stratosphere on the trapped wave train: 1) the wave amplitude, particularly over the first three wavelengths, is significantly stronger with a stratosphere than in the no-stratosphere (two-layer) case, and 2) the trapped waves in the strong-stratosphere case maintain at least as much amplitude as those in the no-stratosphere case, suggesting that the upward leakage of wave energy into the highly stable stratosphere is almost negligible. Each of these behaviors will be investigated in more detail below.

a. Increase in wave amplitude

It has long been established that the amplitude of most trapped lee waves is poorly estimated by linear theory because they are not forced directly by the mountain, but through a nonlinear interaction with the vertically propagating waves forced by the topography (Smith 1976; Nance and Durran 1997). The amplification of the lee waves by the presence of a stratosphere in the preceding simulations may, therefore, be due to the influence of the stratosphere on the vertically propagating wave components. Previous studies have documented that mountain-wave amplitudes are strongly sensitive to the strength and location of the tropopause. Klemp and Lilly (1975) developed a linear three-layer model to evaluate the sensitivity of hydrostatic vertically propagating waves to changes in each layer's depth, stability, and wind shear. Durran (1992) evaluated two-layer solutions to the hydrostatic Long's equations and confirmed that finite-amplitude waves also exhibit a strong sensitivity to the strength and location of layer interfaces, but noted that quantitative amplitude predictions from linear theory may lose their validity at relatively small nondimensional mountain heights in layered atmospheres.

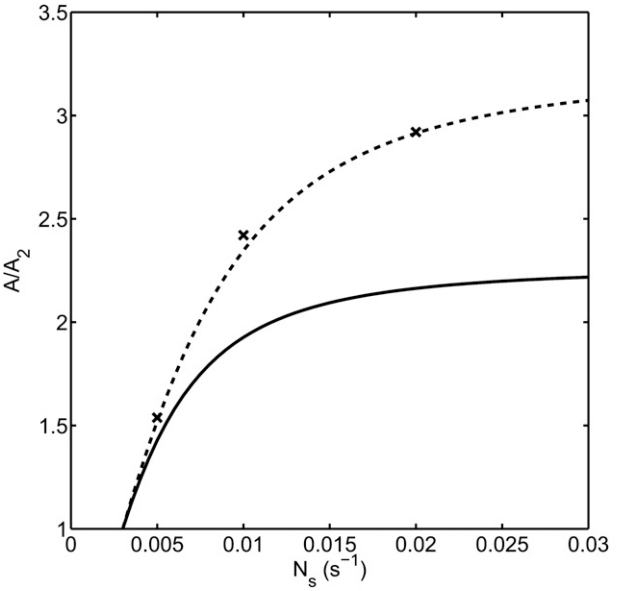

FIG. 12. Three-layer amplification factors as a function of stratospheric static stability N_s, normalized by the amplification factor A_2 from the two-layer no-stratosphere case. Solid line is the theoretical value from Klemp and Lilly (1975); dashed line is the theoretical value using the finite-amplitude adjustment of Durran (1992). Crosses show model results for the isolated-jet case at $t = 19$ h.

The relative strengths of the vertical velocities in simulations with different stratospheric stabilities N_s are compared in Fig. 12. Vertical velocities are taken from each simulation at the location of the first downdraft after the first updraft downstream of the ridge at the time when the peak large-scale flow arrives at this downdraft's location. The vertical velocity is evaluated at the nominal quarter-wavelength level $z = \pi U_m/(2N_l)$ where $U_m = 20$ m s^{-1} is the maximum large-scale wind speed. The vertical velocity in the linear model at the quarter-wavelength level is evaluated using (2) of Klemp and Lilly (1975), and the amplification of this w relative to that in the uniform-N case is given by the factor A in their (8). The theoretically and numerically computed w values are normalized by the value obtained in the two-layer no-stratosphere case, for which $N_s = N_u = 0.003$ s^{-1}. Letting A_2 be the amplification in the no-stratosphere case, the quantities plotted in Fig. 12 are values of A/A_2.

The solid curve in Fig. 12 shows A/A_2 as predicted by the three-layer linear model. The crosses show results for the isolated-jet case with $N_s = 0.005$, 0.01, and 0.02 s^{-1}. The agreement with linear theory is not particularly good, but much better results are obtained using the empirical correction for finite amplitude suggested in Durran (1992), in which $3h/2$ is subtracted from the lower-layer depth used in the tuning calculations (dashed curve). The good agreement with theory, as adjusted for finite amplitude,

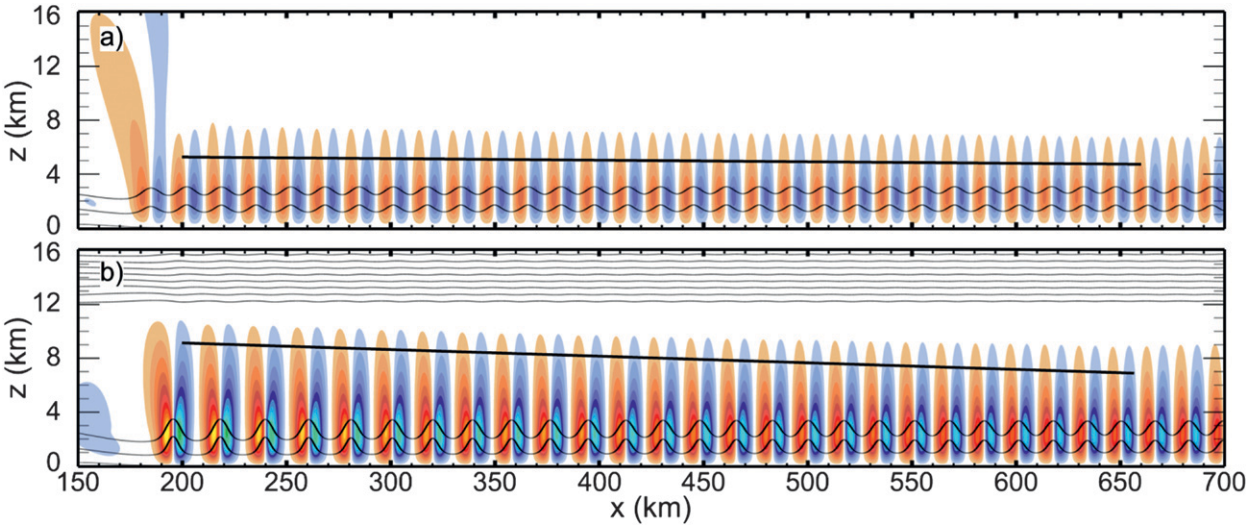

FIG. 13. As in Fig. 2, but for steady, 2D trapped waves at hour 45, with $u = 15$ m s^{-1}. Thick black line illustrates rate of decay of wave amplitude. (a) No-stratosphere case and (b) strong-stratosphere case.

suggests that the increased initial strength of the trapped waves in the strong-stratosphere simulation is due to the constructive superposition of the vertically propagating mountain wave and its partial reflection from the tropopause.[6]

b. *Leakage of wave energy*

Resonant lee waves, which are completely trapped by the low static stability in the upper layer in the no-stratosphere case, can leak energy upward when the two lower layers are topped by a stable stratosphere. Leakage of energy upward through the stratosphere has often been regarded as the primary mechanism through which atmospheric lee waves actually decay, and indeed observations show such waves typically occur in atmospheric structures that permit upward leakage (Brown 1983; Shutts 1992; Georgelin and Lott 2001). More recently, Smith et al. (2002), Jiang et al. (2006), and Smith et al. (2006) have presented observations and analysis showing that lee waves may also be dissipated by interactions with critical levels near the surface in stagnant boundary layers. Nevertheless, the ultimate fate of trapped lee waves has received relatively little study, and there is no generally accepted understanding of the relative importance of the various factors responsible for their dissipation.

The damping effects of upward energy leakage are apparent in Fig. 13, which compares mature wave trains generated in a 2D (x–z) domain by a steady 15 m s^{-1} flow in the presence of the no-stratosphere and strong-stratosphere thermodynamic profiles. Except for the 2D domain and the steady flow, all physical and numerical parameters in these simulations are identical to those used in the cases forced by the translating isolated jet. As in the previous cases, the trapped waves are stronger in the presence of the stratosphere; however, their amplitude decays downstream faster (with a 37% decrease in wave amplitude over a distance of 500 km) than in the case with no stratosphere (in which there is a 10% decrease over the same distance decrease due to numerical smoothing).

Following wave packets, relative rates of decay are compared for various strong-stratosphere and no-stratosphere combinations in Fig. 14; the cases considered are the steady 2D, the uniform-unsteady, and the isolated-jet simulations. The quantity plotted in Fig. 14 is the magnitude of the normalized vertical velocity $|w/w_0|$ at $z = 3$ km following wave packets launched at hour 16.5 over the 6-h period between hours 23 and 29, a period when they are free of direct interaction with the terrain. Here w is evaluated at $z = 3$ km and w_0 is the value of w at hour 23.

As is apparent in Fig. 14, the steady 2D cases exhibit the least loss in wave amplitude—just 3.4% in the no-stratosphere case (produced by numerical dissipation) and 12.5% in the strong-stratosphere case (due to the combined effects of leakage and numerical dissipation). In contrast, the lateral dispersion of energy in the waves generated by the finite-length ridge leads to a substantial loss of amplitude in the waves along the centerline in the uniform-unsteady case, with the no-stratosphere and strong-stratosphere cases respectively losing 62% and 68% of their original amplitude. Nevertheless, the ratio

[6] Even with the empirical finite-amplitude correction, the excellent agreement with the numerical simulations may be somewhat serendipitous since the underlying theory is for 2D steady waves.

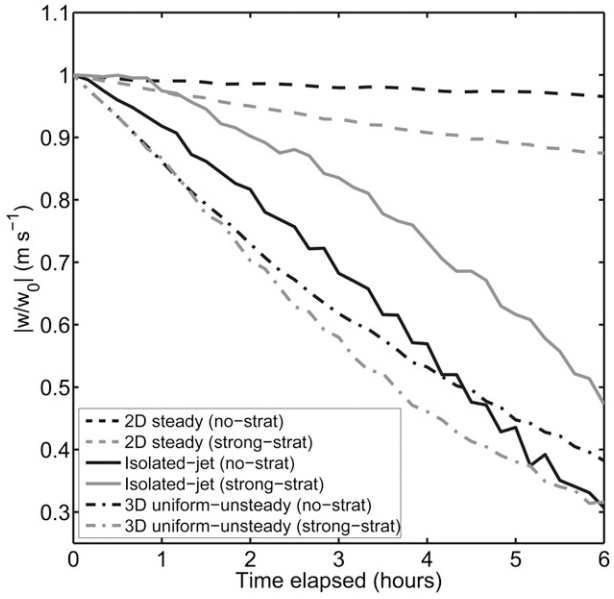

FIG. 14. Normalized vertical velocity along the ray path of the wave packet launched at hour 16.5 for the 2D steady, isolated-jet and the 3D uniform-unsteady simulations during the period between hours 23 and 29. Black lines: no-stratosphere case; gray lines: strong-stratosphere case.

of the final amplitude in the no-stratosphere case to that in the strong-stratosphere case remains similar in the steady 2D and the uniform-unsteady 3D simulations, suggesting that leakage into the stratosphere is proceeding at a similar rate in both situations.

The influence of the stratosphere on the dissipation rates in the isolated-jet case is, however, reversed. Waves along the centerline in the strong-stratosphere case lose just 52% of their amplitude, while those in the no-stratosphere case lose 69%. In contrast to the other cases, the presence of the stratosphere helps maintain the amplitude of the trapped waves, a surprising result that is the subject of continued investigation. The tendency of the waves in both isolated-jet simulations to decay more slowly than those in the uniform-unsteady case over the first 4 h appears to be produced by horizontal confluence in the mean flow while the waves are located upstream of the jet maximum. Decay of the waves increases once they lie in the divergent region downwind of the jet maximum.[7]

[7] The average wavelength for these wave packets is 15.8 km in the no-stratosphere steady 2D case, 29.7 km in the uniform-unsteady case, and, according to the WKB analysis, changes from 19.8 km at hour 23 to 17.2 km at hour 29 in the isolated-jet case. Since the 2D wavelengths are shortest, dissipation of waves by numerical smoothing does not explain the enhanced rate of decay in the 3D simulations.

8. Similarity to observations

A widespread trapped wave event occurred downwind of the Cascade Range in Washington and Oregon on 5 May 2011. Mature lee waves were well developed downwind of several sections of the range by midmorning. Rapid decay of the waves subsequently proceeded in a similar manner to that outlined in this study. This event is analyzed using 1-km Geostationary Operational Environmental Satellite-West (GOES-W) visible imagery, standard radiosonde soundings at Quillayute and Spokane, Washington, and at Salem, Oregon, analysis charts, and operational forecasts generated by the University of Washington Weather Research and Forecasting–Global Forecast System (WRF-GFS) Model run at 4/3-km horizontal resolution and initialized at 1200 UTC 5 May 2011.

Figure 15 shows a series of four satellite images taken at 15-min intervals between 1900 and 1945 UTC, focused on the wave train in the area of the Columbia River. During this 45-min period, the third, fourth, fifth, and sixth trapped wave crests progressively decay while waves persist farther downstream, creating a gap in the wave train similar to that modeled in our study. The first two waves in the immediate lee of the terrain remain undamped. Decay of the waves initially occurs close to the terrain and quickly spreads downwind with time. Waves farther downstream persist longer, although they too eventually decay in the following 2 h, and again decay occurs from west (upwind) to east (downwind). Similar decay occurs at other locations along the ridge, although the exact structure is harder to discern elsewhere due to less coherent waves and other cloud layers. Following this decay, vertically propagating waves over the area are clearly visible in satellite imagery (not shown).

Figure 16 shows a sounding taken upwind at Salem at 0000 UTC 6 May 2011, shortly after the time of apparent untrapping. The structure of the atmosphere shown in Fig. 16 is still favorable for trapped waves, with a deep isothermal layer between 750 and 650 hPa and weaker static stability aloft, 25 knots (kt; 1 kt = 0.51 m s^{-1}) of cross-mountain flow, and a significant increase in the cross-mountain winds with height. The low levels are moist so lee waves should be made visible by clouds. Similar thermodynamic structures are seen elsewhere in the Pacific Northwest at this time (Quillayute and Spokane), suggesting that the disappearance of the wave clouds in Fig. 15 is not due to major changes in atmospheric structure or humidity.

The WRF-GFS Model also forecast trapped lee waves in this location—approximately six wave crests were evident, with a similar distribution and wavelength to those observed in the satellite imagery. However, the downstream extent of waves in the model was shorter

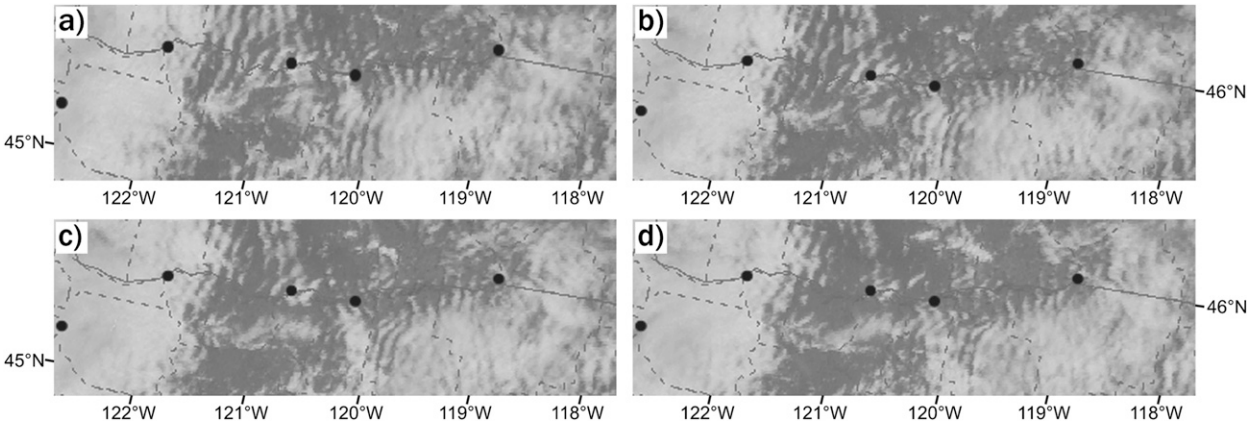

FIG. 15. GOES-W visible images showing trapped waves along the Columbia River in the lee side of the Cascade Mountains at (a) 1900, (b) 1915, (c) 1930, and (d) 1945 UTC. Black dots indicate locations of, from west to east, Aurora, OR, Cascade Locks, OR, Maryhill, WA, Arlington, OR, and Port Kelly, WA.

than observed, likely due to numerical damping in the model. Waves decayed and became vertically propagating in the model at a similar time to those in the satellite imagery. In addition, model sounding profiles agree well with observations. Given this good agreement, we use WRF Model soundings to estimate the spatial gradients and temporal evolution of the wind field along a cross section through the wave train following the Columbia River. Unfortunately, the archived WRF Model data were only available at 3-h resolution at predetermined locations, and the archived wind speed is only available rounded to the nearest multiple of 5 kt.

Figure 17 shows the WRF Model wind speeds at 850 hPa along a transect perpendicular to the waves at 1500, 1800, and 2100 UTC (similar results are seen at other levels in the lower troposphere). Values are taken at, from west to east, Aurora, Oregon, Cascade Locks, Oregon, Maryhill, Washington, Arlington, Oregon, and Port Kelly, Washington—the five points marked in Fig. 15. As the wave train was developing and maturing at 1500 UTC, background wind speeds were uniform at 20 kt along the wave train (to the ±5-kt accuracy of the archived winds). After this time, the winds closest to the mountain weaken, while those downwind at Maryhill and Arlington increase. During this period, satellite images show that the wavelength of these waves increases at roughly 9% h^{-1}.[8] Figure 18 shows lengthening of the wavelength was also present prior to wave decay in the WRF Model, with an increase of approximately 8% h^{-1} between 1700 and 1900 UTC. At both 1800 and 2100 UTC, a region where $\partial\overline{u}/\partial x > 0$ has developed, extending from just upwind of the terrain to about 150 km downwind of the crest. In contrast, beyond 150 km, $\partial\overline{u}/\partial x$ has become negative. A comparison of these variations in $\partial\overline{u}/\partial x$ with the wave structure shown in Fig. 15 shows that the waves that decay are indeed in the region where $\partial\overline{u}/\partial x > 0$, and waves farther downwind that persist are in the area where $\partial\overline{u}/\partial x < 0$. Consequentially, it appears that the trapped waves in this event behaved and evolved similarly to those in our model, and likely became untrapped and decayed through the same underlying mechanism. It is possible that additional terrain downstream of the Cascades may be impacting the wave train in a manner that we cannot study using the available data. However until Port Kelly the lee-side topography

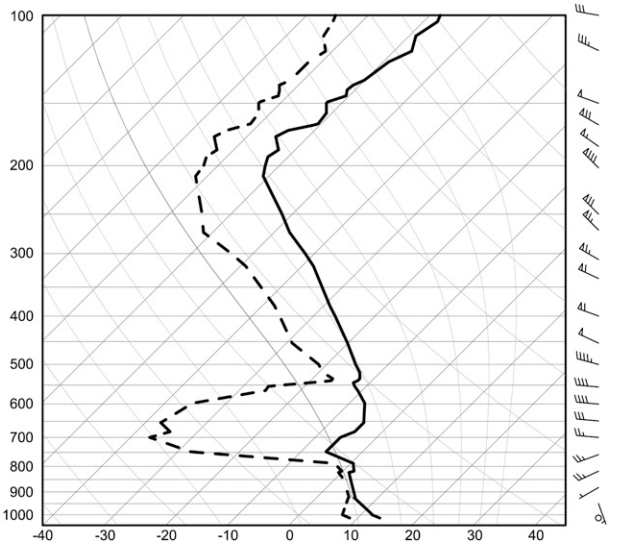

FIG. 16. Salem, OR, sounding at 0000 UTC 6 May 2011.

[8] The satellite images documenting the shorter waves at earlier times are difficult to reproduce because of low sun angle and the presence of some high clouds.

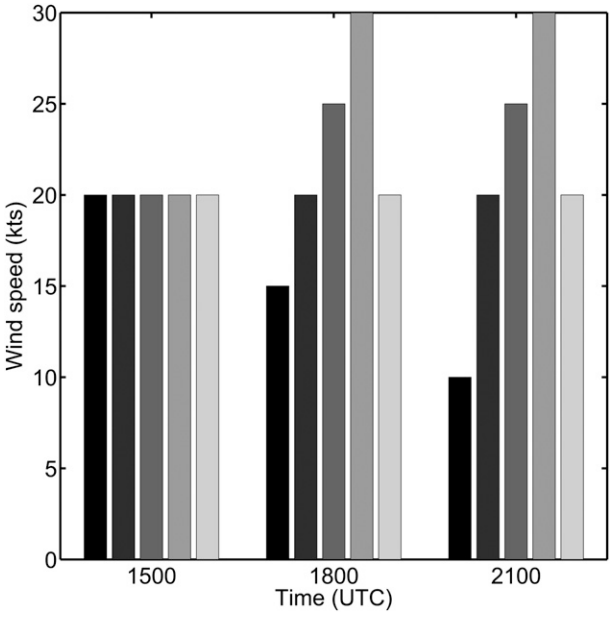

FIG. 17. Wind speeds at 850 hPa predicted by the WRF Model and archived to the nearest 5 kt for the synthetic sounding locations shown by the black dots in Fig. 15 at 1500, 1800, and 2100 UTC. Data are plotted in order from west to east.

is relatively flat and, since the flow has a dominant westerly component, we expect lee-side terrain impacts to be minimal.

9. Conclusions

Atmospheric flows are never completely steady, and changes in the speed of the large-scale flow are almost always associated with horizontal gradients in the velocity field. In this study we have examined the behavior of trapped waves triggered by an isolated barotropic jet passing over a ridge of finite length. The flow accelerates from rest to a maximum of 20 m s^{-1} and then returns to rest over a period of 33.3 h; the wavelength of the perturbation associated with the jet is 1200 km. Despite the relatively long time- and spatial-scale variations in the large-scale flow, the behavior of the lee waves triggered by this jet is dramatically different from that generated by either a steady flow or by a horizontally uniform unsteady flow whose velocity everywhere matches the instantaneous velocity at the ridge crest in the case with the isolated jet.

As the flow above the mountain accelerates, the initial development of the lee waves is similar to that in an impulsively started steady flow, with the wave train slowly expanding downstream. However, the simulated waves differ substantially from those generated by impulsively started steady flows after the jet maximum passes over the mountain. Those trapped waves that remain in the region downwind of the jet maximum (where $\partial\overline{u}/\partial x < 0$) tend to remain trapped as their wavelength decreases, and they continue to propagate downstream just ahead of the jet maximum. In contrast, those waves overtaken by the jet maximum or generated upwind of the jet max (which exist in an environment where $\partial\overline{u}/\partial x > 0$) tend to become untrapped and decay as their wavelength gradually increases. The region of decaying waves expands downstream with time and eventually leaves a gap between a pair of waves near the mountain crest and those downstream of the jet maximum.

The simulated response of wave packets to variations in the large-scale flow is in quantitative agreement with the results obtained using WKB ray tracing, thereby providing theoretical support for our identification of large-scale spatial gradients as the agents responsible for the modeled changes in wavelength and intrinsic frequency. The key role played by such gradients was confirmed by comparing the isolated-jet cases with simulations of horizontally uniform unsteady flows. Once launched, the waves in the uniform-unsteady simulations conserve their wavelength and simply slide back and

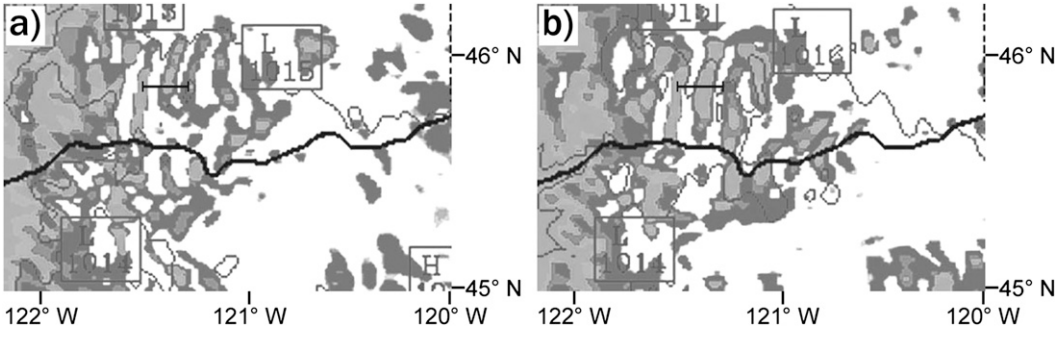

FIG. 18. WRF Model simulation at (a) 1700 and (b) 1900 UTC. Shading shows the cloud water field. Contours are for surface pressure; thick line is the Columbia River. Line segment terminated with tick marks is the same length in each panel.

forth with respect to the mountain as the large-scale flow first accelerates and then returns to zero.

In both the isolated-jet and uniform-unsteady cases, the wavelength at which the trapped waves are launched steadily increases with time. Trapped wave generation ceases before the arrival of large-scale conditions that might lead to a steady decrease in the initial wavelength. The rate of increase in wavelength is comparable to the average value obtained by Ralph et al. (1997) in a survey of 24 real-world events. Ralph et al. (1997) attributed the tendency of the wavelength to grow with time to diurnal heating of the planetary boundary layer, but it is possible that the behavior identified here is also a contributing factor.

Satellite imagery and high-resolution WRF Model data relating to a trapped wave event over Washington and Oregon provide a potential example of real-world trapped waves behaving similarly to those in our idealized simulations. Four wavelengths of the mature wave train decay progressively from west to east, while waves further downstream persist. Wind fields from the WRF Model simulation show that the observed and simulated waves decay in a region where $\partial\overline{u}/\partial x$ has become positive, and in agreement with our results, the wavelength of the lee waves increases in this region at an average rate of 8% h^{-1}. On the other hand, $\partial\overline{u}/\partial x < 0$ in the region where the waves persist.

The influence of the stratosphere on the trapped waves in the isolated-jet cases is complex. The waves are stronger in the presence of a stratosphere than in a strictly two-layer atmosphere, even though the two-layer configuration prevents any upward leakage of wave energy. First, the waves are triggered at larger initial amplitudes through nonlinear interactions with vertically propagating waves that have been amplified by partial reflections at the tropopause in the strong-stratosphere case. Second, as waves propagate downstream in the presence of a strong stratosphere, they lose significantly less amplitude than those in the corresponding no-stratosphere (two-layer) case. This unexpected resistance to upward energy leakage stands in contrast to our other simulations in which leakage into the stratosphere was an important dissipation mechanism in both steady two-dimensional and three-dimensional uniform-unsteady flows. We are continuing to investigate the reasons why trapped waves decay more slowly in the isolated-jet case when a stable stratosphere is present.

Acknowledgments. The authors are grateful for helpful conversations with Oliver Bühler. This research was supported by National Science Foundation Grants ATM-0836316 and AGS-1138977. This work was facilitated through the use of advanced computational, storage, and networking infrastructure provided by the Hyak supercomputer system, supported in part by the University of Washington eScience Institute.

REFERENCES

Bougeault, P., 1983: A non-reflective upper boundary condition for limited-height hydrostatic models. *Mon. Wea. Rev.,* **111,** 420–429.

Bretherton, F. P., 1969: Momentum transport by gravity waves. *Quart. J. Roy. Meteor. Soc.,* **95,** 213–243.

Broad, A. S., 2002: Momentum flux due to trapped lee waves forced by mountains. *Quart. J. Roy. Meteor. Soc.,* **128,** 2167–2173.

Brown, P. R. A., 1983: Aircraft measurements of mountain waves and their associated momentum flux over the British Isles. *Quart. J. Roy. Meteor. Soc.,* **109,** 849–865.

Bühler, O., 2009: *Waves and Mean Flows*. Cambridge University Press, 341 pp.

Chen, C.-C., D. R. Durran, and G. J. Hakim, 2005: Mountain-wave momentum flux in an evolving synoptic-scale flow. *J. Atmos. Sci.,* **62,** 3213–3231.

——, G. J. Hakim, and D. R. Durran, 2007: Transient mountain waves and their interaction with large scales. *J. Atmos. Sci.,* **64,** 2378–2400.

Doyle, J., and D. R. Durran, 2002: The dynamics of mountain-wave-induced rotors. *J. Atmos. Sci.,* **59,** 186–201.

Durran, D. R., 1992: Two-layer solutions to Long's equation for vertically propagating mountain waves: How good is linear theory? *Quart. J. Roy. Meteor. Soc.,* **118,** 415–433.

——, 1995: Do breaking mountain waves decelerate the local mean flow? *J. Atmos. Sci.,* **52,** 4010–4032.

——, 2010: *Numerical Methods for Fluid Dynamics with Applications to Geophysics.* Springer, 516 pp.

——, and J. B. Klemp, 1983: A compressible model for the simulation of moist mountain waves. *Mon. Wea. Rev.,* **111,** 2341–2361.

Epifanio, C. C., and D. R. Durran, 2001: Three-dimensional effects in high-drag-state flows over long ridges. *J. Atmos. Sci.,* **58,** 1051–1065.

Georgelin, M., and F. Lott, 2001: On the transfer of momentum by trapped lee waves: Case of the IOP 3 of PYREX. *J. Atmos. Sci.,* **58,** 3563–3580.

Holmboe, J., and H. Klieforth, 1957: Investigations of mountain lee waves and airflow over the Sierra Nevada. Final Rep., Contract AF19(604)-728, Dept. of Meteorology, University of California, Los Angeles, 290 pp.

Jiang, Q., J. D. Doyle, and R. B. Smith, 2006: Interaction between trapped waves and boundary layers. *J. Atmos. Sci.,* **63,** 617–633.

Klemp, J. B., and D. K. Lilly, 1975: The dynamics of wave induced downslope winds. *J. Atmos. Sci.,* **32,** 320–339.

——, and D. R. Durran, 1983: An upper boundary condition permitting internal gravity wave radiation in numerical mesoscale models. *Mon. Wea. Rev.,* **111,** 430–444.

Lilly, D. K., 1962: On the numerical simulation of buoyant convection. *Tellus,* **14,** 148–172.

Lindsay, C. V., 1962: Mountain waves in the Appalachians. *Mon. Wea. Rev.,* **90,** 271–276.

Lott, F., and H. Teitelbaum, 1993a: Linear unsteady mountain waves. *Tellus,* **45A,** 201–220.

——, and ——, 1993b: Topographic waves generated by a transient wind. *J. Atmos. Sci.,* **50,** 2607–2624.

Mitchell, R. M., R. P. Cechet, P. J. Turner, and C. C. Elsum, 1990: Observation and interpretation of wave clouds over

Macquarie Island. *Quart. J. Roy. Meteor. Soc.,* **116,** 741–752.

Nance, L. B., and D. R. Durran, 1997: A modelling study of nonstationary trapped mountain lee waves. Part I: Mean-flow variability. *J. Atmos. Sci.,* **54,** 2275–2291.

——, and ——, 1998: A modeling study of nonstationary trapped mountain lee waves. Part II: Nonlinearity. *J. Atmos. Sci.,* **55,** 1429–1445.

Queney, P., G. A. Corby, N. Gerbier, H. Koschmieder, and J. Zierep, 1960: The airflow over mountains. WMO Tech. Note 34, 135 pp.

Ralph, F. M., M. Crochet, and S. V. Venkateswaran, 1992: A study of mountain lee waves using clear-air radar. *Quart. J. Roy. Meteor. Soc.,* **118,** 597–627.

——, P. J. Neiman, T. L. Keller, D. Levinson, and L. Fedor, 1997: Observations, simulations and analysis of nonstationary trapped lee waves. *J. Atmos. Sci.,* **54,** 1308–1333.

Richard, E., P. Mascart, and E. C. Nickerson, 1989: The role of surface friction in downslope windstorms. *J. Appl. Meteor.,* **28,** 241–251.

Scorer, R., 1949: Theory of waves in the lee of mountains. *Quart. J. Roy. Meteor. Soc.,* **75,** 41–56.

Sharman, R., and M. Wurtele, 2004: Three-dimensional structure of forced gravity waves and lee waves. *J. Atmos. Sci.,* **61,** 664–681.

Shutts, G. J., 1992: Observations and numerical model simulation of a partially trapped lee wave over the Welsh Mountains. *Mon. Wea. Rev.,* **120,** 2056–2066.

Smith, R. B., 1976: The generation of lee waves by the Blue Ridge. *J. Atmos. Sci.,* **33,** 507–519.

——, S. Skubis, J. D. Doyle, A. S. Broad, C. Kiemle, and H. Volkert, 2002: Mountain waves over Mont Blanc: Influence of a stagnant boundary layer. *J. Atmos. Sci.,* **59,** 2073–2092.

——, Q. Jiang, and J. D. Doyle, 2006: A theory of gravity wave absorption by a boundary layer. *J. Atmos. Sci.,* **63,** 774–781.

Starr, J. R., and K. A. Browning, 1972: Observations of lee waves by high-power radar. *Quart. J. Roy. Meteor. Soc.,* **98,** 73–85.

Vergeiner, I., and D. K. Lilly, 1970: The dynamic structure of lee wave flow as obtained from balloon and airplane observations. *Mon. Wea. Rev.,* **98,** 220–232.

Vosper, S., and R. Worthington, 2002: VHF radar measurements and model simulations of mountain waves over Wales. *Quart. J. Roy. Meteor. Soc.,* **128,** 185–204.

Whitham, G. B., 1974: *Linear and Nonlinear Waves.* Wiley-Interscience, 656 pp.

Worthington, R. M., and L. Thomas, 1996: Radar measurements of critical-layer absorption in mountain waves. *Quart. J. Roy. Meteor. Soc.,* **122,** 1263–1282.

Wurtele, M. G., 1955: The transient development of a lee wave. *J. Mar. Res.,* **14,** 1–13.

——, A. Datta, and R. Sharman, 1999: Unsteadiness and periodicity in gravity waves and lee waves forced by a fixed rigid boundary. *J. Atmos. Sci.,* **56,** 2269–2276.